

MRI Information-Based Correction and Restoration of Photoacoustic Tomography

Shuangyang Zhang^{ID}, Li Qi^{ID}, Xipan Li^{ID}, Zhichao Liang, Xiangdong Sun, Jiaming Liu, Lijun Lu^{ID}, Yanqiu Feng^{ID}, and Wufan Chen^{ID}, Senior Member, IEEE

Abstract—As an emerging molecular imaging modality, Photoacoustic Tomography (PAT) is capable of mapping tissue physiological metabolism and exogenous contrast agent information with high specificity. Due to its ultrasonic detection mechanism, the precise localization of targeted lesions has long been a challenge for PAT imaging. The poor soft-tissue contrast of the PAT image makes this process difficult and inaccurate. To meet this challenge, in this study, we first make use of the rich and clear structural information brought about by another advanced imaging modality, Magnetic Resonance Imaging (MRI), to assist organ segmentation and correct for the light fluence attenuation of PAT. We demonstrate improved feature visibility and enhanced localization of endogenous and exogenous agents in the fluence corrected PAT images. Compared with PAT-based methods, the contrast-to-noise ratio (CNR) of our MRI-assisted method increases by 29.1% in live animal experiments. Furthermore, we show that the co-registered MRI image can also be incorporated into PAT image restoration, and achieves improved anatomical landscape and soft-tissue contrast (CNR increased by 25.36%) while preserving similar spatial resolution. This PAT-MRI combination provides excellent structural, functional and molecular images of the subject, and may enable more comprehensive analysis of various preclinical research applications.

Index Terms—Photoacoustic tomography, magnetic resonance imaging, soft-tissue contrast, light fluence.

I. INTRODUCTION

POTOACOUSTIC tomography (PAT), or optoacoustic tomography (OAT), as an emerging biomedical molecular

Manuscript received 1 February 2022; revised 28 March 2022; accepted 4 April 2022. Date of publication 8 April 2022; date of current version 31 August 2022. This work was supported in part by the Guangdong Basic and Applied Basic Research Foundation under Grant 2021A1515012542 and Grant 2022A1515011748, in part by the Guangdong Pearl River Talented Young Scholar Program under Grant 2017GC010282, and in part by the Key-Area Research and Development Program of Guangdong Province under Grant 2018B030333001. (Corresponding authors: Li Qi; Wufan Chen.)

This work involved human subjects or animals in its research. Approval of all ethical and experimental procedures and protocols was granted by the Laboratory Animal Ethics Committee, Southern Medical University.

The authors are with the School of Biomedical Engineering, Southern Medical University, also with the Guangdong Provincial Key Laboratory of Medical Image Processing, Southern Medical University, and also with the Guangdong Province Engineering Laboratory for Medical Imaging and Diagnostic Technology, Southern Medical University, Guangzhou 510515, China (e-mail: syzhang@smu.edu.cn; qili@smu.edu.cn; 1036317406@qq.com; 2153136120@qq.com; sunxiangdong2013@163.com; jiaming_liu@smu.edu.cn; lulijun@smu.edu.cn; foree@163.com; chenwf@smu.edu.cn).

Digital Object Identifier 10.1109/TMI.2022.3165839

imaging modality, is able to reveal the distribution of the optical absorption characteristics in real-time with optical contrast and ultrasonic spatial resolution [1]–[3]. In PAT, an image that maps the original energy deposition inside the target is formed by detecting and processing the ultrasonic signals generated by laser illumination. Thanks to the specific optical absorption spectra of chromophores, multispectral PAT that utilized multiple wavelength excitation can distinguish the distribution of endogenous tissue absorbers, such as oxyhemoglobin (HbO_2) and de-oxyhemoglobin (Hb), and exogenous optical probes such as the FDA-approved Indocyanine Green (ICG) by identifying their absorption spectrum [4], [5]. The distribution of these functional PAT biomarkers is crucial for locating and understanding the physiological information of different lesions [6].

However, due to the inherent low soft-tissue contrast of PAT, it is considered difficult to identify both the anatomical location and concentration of the chromophores [7]–[12]. Besides, PAT images can only qualitatively provide the absorbed light energy density distribution, which is the product of the absorption coefficient and the light fluence (LF) distribution [13]. The tissue absorption coefficient, as an inherent attribute, is closely related to the structural and functional information. Eliminating the LF from the PAT image and recovering the distribution of the optical absorbers are of great interest.

Previous attempts to correct for this LF effect started from the PAT image solely [14]–[17]. These methods involved dividing the image to organ level and optimizing the optical parameters of each region in order to solve for the LF distribution [17]. However, the unclear soft-tissue structure of the PAT image is likely to generate segmentation errors. Also, dividing the LF map will simultaneously amplify noise and thus affect correction accuracy. Regularization methods, such as the total-variation approach [18], have been proposed to improve PAT image quality by suppressing noise and inherent PAT imaging artifacts including the streaking artifacts [5]. However, extracting the true gradient information of the anatomy is difficult and thus the performance of the algorithm is limited.

As an advanced imaging modality widely used in both clinical and pre-clinical researches, Magnetic Resonance Imaging (MRI) is able to provide excellent anatomical definition and soft tissue contrast. This makes it possible to help improve target lesion positioning and analysis of PAT. Previously, image registration of these two modalities included manual registration and rigid registration [19]–[25], but were limited

by poor registration accuracy and the type of application (e.g. brain imaging). Recently, a proof-of-concept parallel PAT-MRI imaging system has been proposed with phantom-based feasibility validation [26]. Development of such system requires high-cost customized instruments and sacrifices the flexibility of individual system. Recently, our group proposed a complete hardware-software solution for the successive acquisition and co-registration of PAT and MRI images in *in vivo* animal studies [27]. The design of the dual-modality animal imaging bed ensures that the deformation of the animal is within acceptable range when switching imaging modalities, thereby simplifying image co-registration. In despite of these efforts to integrate MRI with PAT, the potential function for using MRI to improve PAT imaging has not been delving into yet.

Based on this, here we propose a method for MRI information-based correction and restoration of PAT in small animal *in vivo* imaging studies. By making use of the rich and clear structural information brought about by MRI to perform refined organ segmentation, we obtain a more accurate estimation of the LF attenuation for PAT images, and thus enhance the structural visibility of imaging details. Furthermore, we show that incorporating the MRI image into PAT image restoration by using image gradient information achieves improved soft-tissue contrast and anatomical landscape. We use simulation and live animal experiments to demonstrate that the combination with MRI is capable of removing the aforementioned limitation in PAT imaging and enables accurate positioning and analysis of the targeted lesion. Our proposed MRI-PAT dual-modality imaging provides structural, functional, and molecular images simultaneously, and therefore allows for broader and more precise analysis of different pre-clinical research applications.

II. THEORY

A. LF Model of PAT

The PAT images are formed by reconstructing the original point source of the ultrasonic waves generated by absorbing the laser pulse, and the pixel value $p(\vec{r})$ in the image is expressed as:

$$p(\vec{r}) = \alpha \Gamma \mu_a(\vec{r}) \Phi[(\vec{r}), \mu_a(\vec{r}), \mu'_s(\vec{r})], \quad (1)$$

where α denotes the system response, Γ denotes the thermo-elastic Grüneisen parameter, $\mu_a(\vec{r})$ and $\mu'_s(\vec{r})$ denote the absorption coefficient and the scattering coefficient, and Φ denotes the LF within a voxel at the position \vec{r} . In the beginning, we make the reasonable assumption that $p(\vec{r})$ has been reconstructed from the acoustic measurements accurately and with negligible structural distortion [5], [18], [28]. In biological soft tissue, the thermo-elastic Grüneisen parameter has a small variation so that it is assumed to be constant [17]. Then, the distribution of absorbed energy $p'(\vec{r})$ is obtained by eliminating the constant terms from $p(\vec{r})$. Finally, the PAT image p' can be expressed as the product of the LF distribution Φ and the absorption coefficient μ_a :

$$p' = \Phi(\mu_a, \mu'_s) \cdot \mu_a. \quad (2)$$

Compensation of the fluence effect is performed by first calculating the LF distribution of the laser over the entire imaging object and then dividing the PAT image by the obtained LF map. However, obtaining the solution of the LF distribution Φ from equation (2) is considered difficult because it depends on both the absorption coefficient μ_a and the scattering coefficient μ'_s , although it is often assumed that μ'_s is known [14], [29]–[31].

B. PAT-Segmentation-Based LF Correction Algorithms

The correct absorption and scattering coefficients should be assigned to different tissue to initialize LF estimation, and identifying different tissue requires image segmentation. For example, Mandal *et al.* proposed an LF correction method based on PAT contour segmentation [30], which we termed PAT-CS. This method segments the object contour and assumes uniform optical parameters within the imaged object, and the LF map is estimated by manually selecting the absorption coefficient μ_a and the scattering coefficient μ'_s . Thus, its accuracy depends on the choice of the optical parameters. Brochu *et al.* later proposed an LF correction method based on PAT organ segmentation (we termed PAT-OS) to improve LF estimation accuracy [17]. This method iteratively calculates the optical parameters to minimize the error between the raw PAT image and an estimated PAT image, which equals to the product of the LF map and the absorption coefficient map. However, the poor soft-tissue contrast of PAT images makes organ segmentation very difficult.

C. The Proposed LF Correction Algorithm

Here, we proposed an LF correction method based on MRI organ segmentation (MRI-OS). Our method, as shown in Fig. 1(c), used co-registered MRI (rMRI) images as prior information to segment the object from the organ level into several regions R_N . Each of these regions exhibited small changes in its content, and therefore the absorption coefficient within an individual region was considered to be uniform. Compared to the PAT-OS method which is also based on organ segmentation, our method uses MRI images to perform more refined delineation of organ boundaries, and thus has the potential to improve LF correction effect.

With equation (2), the imaging model can be represented as a nonlinear model:

$$p' = \Phi(\mu_a) \mu_a, \quad (3)$$

where p' and μ_a are the PAT image and the absorption coefficient in vector representation, Φ is the LF in sparse matrix representation. Then, LF correction can be carried out as a least squared optimization problem as:

$$\hat{\mu}_a = \arg \min \| p' - \Phi(\mu_a) \mu_a \|^2. \quad (4)$$

The direct solution of the above objective function is difficult because the LF matrix Φ depends on μ_a . Instead of using un-customized optimization functions in commercial software as in Reference [17], we developed a two-step optimization method to iteratively calculate the LF distribution. In our

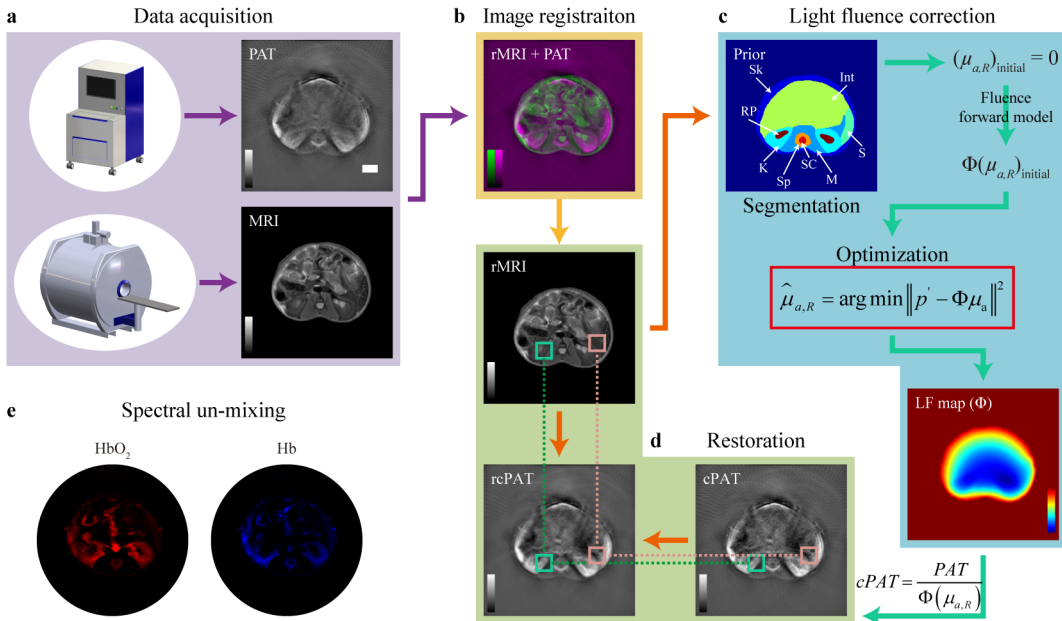


Fig. 1. Schematic diagram of PAT image correction and restoration based on MRI information. (a) Data acquisition. PAT data acquisition: 4-D multi-wavelength multi-slice PAT images are acquired. MRI data acquisition: a 2-D spin echo sequence was used to acquire MRI images. (b) Image registration. A rigid transverse registration on corresponding PAT-MRI image slices are performed. rMRI: registered MRI images. (c) Schematic of the iterative optimization procedure to obtain the optimal optical parameters and perform LF correction. Prior: segmentation result. LF map (Φ): light fluence distribution solved by the proposed optimization program. (d) MRI-information-based image restoration. cPAT: LF corrected PAT image. rcPAT: image restored by our method. (e) Spectral unmixing. The distribution of endogenous (HbO_2 , Hb) absorbers is identified on multispectral PAT images. Description of markers in (c): Sk: skin; Int: intestines; K: kidney; RP: renal pelvis; Sp: spine; SC: spinal cord; M: muscle; S: spleen. Scale bar, 3 mm.

Algorithm 1 Two-Step Iterative Algorithm for LF Correction of PAT

```

Input:  $\mu_{a,R}^{(0)}$ ,  $\mu'_{s,R}$ ,  $k$ , Iter max,  $\varepsilon$ ,  $R_N$ .
Repeat
  1. Update  $\Phi^k$  using the DE with  $\mu_{a,R}^{k-1}$ ,  $\mu'_{s,R}$ .
  2. Update  $\mu \mu_a^k$  by solving  $\mu_a^k = \arg \min \|p' - \Phi^k \mu_a\|^2$ .
  3. Update  $\mu_{a,R}^k$  using:  $\mu_{a,R}^k = \sum_{n=1}^N \frac{\mu_a^k R_n}{\sum R_n} \cdot R_n$ .
  4. Calculate the error:  $err \leftarrow \text{norm} (p' - \Phi^k \mu_{a,R}^k)$ .
  5. Update the iterations:  $k \leftarrow k + 1$ .
Until convergence where  $k > \text{Iter max}$  or  $err < \varepsilon$ .
Calculate  $\Phi^{k+1}$  using the DE with  $\mu_{a,R}^k$ ,  $\mu'_{s,R}$ .
Output:  $\Phi^{k+1}$ .
  
```

method, during each iteration, we first assume a constant μ_a to obtain an initial LF matrix Φ , which in turn converts the objective function into a linear model. Then μ_a is updated from this linear model. These two steps are repeated until convergence. The detail steps of our method are summarized in **Algorithm 1**.

Finally, by dividing the raw PAT image by the LF map, we can obtain the LF corrected PAT image (cPAT):

$$cPAT = \frac{PAT}{\Phi^{k+1}}. \quad (5)$$

In the optimization algorithm, the LF distribution was modeled in the 2D plane by the Diffusion Equation (DE), which was performed in MATLAB (The Mathworks, Inc., USA) using the Toast++ toolbox (Martin Schweiger and Simon

Arridge, Department of Computer Science and the Centre for Medical Image Computing, University College London) [32]. The finite element method was employed in Toast++ to model the light transport inside the object. During the optical transport modeling process, the background medium is set to water.

D. PAT Restoration Based on MRI Information

In PAT image restoration, to integrate prior knowledge into the imaging model, a regularization term $J(x)$ can be added to the classic image restoration function:

$$x' = \arg \min \left\{ \frac{1}{2} \|x - x'\|^2 + \alpha J(x') \right\}, \quad (6)$$

where x is the LF corrected PAT image, x' is the restored image, $\alpha \geq 0$ is the regularization parameter. Previous studies have designed a variety of prior terms to remove artifacts and noise in PAT images [18], [33], especially for sparse sampling PAT [5], [34]. However, the prior image acquired from PAT suffered from poor contrast and unclear structure, which limits the improvement of these algorithms.

In this paper, we use the co-registered MRI images with rich structural information and excellent soft-tissue contrast as prior knowledge. Therefore, the design of the regularization term should introduce the structural features of MRI to PAT, but avoid mixing MRI intensity information. To achieve this, we employ the directional total variation (dT V) algorithm which not only can effectively suppress artifacts and improve clarity, but also better preserves details [35].

The dTV regularization is defined as:

$$J(x) = \sum_{n=1}^N |\nabla x_n - \langle \xi_n, \nabla x_n \rangle \xi_n|, \quad (7)$$

where N is the total pixel number of the image. ξ_n is expressed as:

$$\xi_n = \nabla v_n / |\nabla v_n|_\eta, \quad (8)$$

where v is the registered MRI image. η is edge parameter, which is related to the size of an edge. By using dTV, the PAT image restoration process incorporates the MRI structural information by reducing the penalty for the location of edges extracted from rMRI (green and red boxes in Fig. 1(d)).

E. Spectral Un-Mixing

The reconstructed PA signal is a combination of various endogenous and exogenous absorbers, and there is a linear relationship between the PA signal $\mu_a(\lambda)$ and the absorption coefficient $\mu_a^i(\lambda)$ of the identified chromophore i :

$$\mu_a(\lambda) = \sum_i \mu_a^i(\lambda) = \sum_i c_i \varepsilon_i(\lambda), \quad (9)$$

where, c_i is the concentration of chromophore i and $\varepsilon_i(\lambda)$ is the molar extinction coefficient at λ wavelength. In multispectral PAT, the core idea of spectral separation is to decompose the distribution of each absorber by identifying the specific absorption curve of each absorber [Fig. 1(e)]. In this paper, we choose the most commonly used linear un-mixing method to calculate the distribution of HbO_2 and Hb [36].

After obtaining the concentrations of HbO_2 (c_{HbO_2}) and Hb (c_{Hb}), the $s\text{O}_2$ can be computed as:

$$s\text{O}_2 = \frac{c_{\text{HbO}_2}}{c_{\text{HbO}_2} + c_{\text{Hb}}}. \quad (10)$$

III. EXPERIMENTAL SETUPS AND METHODS

A. Photoacoustic Tomography Imaging

A commercial small animal multispectral optoacoustic tomography system (MSOT inVision128, iThera Medical, Germany) was employed for imaging [Fig. 1(a)]. Pulsed laser (670 nm - 960 nm tunable) with pulse width <10 ns, repetition rate of 10 Hz, and a peak pulse energy of 60 mJ at 760 nm excite the sample through a ten-arm fiber bundle, which provides homogeneous, 360-degree illumination of approximately 8 mm width over the surface of the sample. The generated ultrasonic waves are detected by 128 cylindrically focused ultrasound transducers with a center frequency of 5 MHz (60% bandwidth) arranged over an azimuth span of 270-degrees around the cylinder with a radius of curvature of 40.05 mm. MSOT images were averaged with signals from 10 frames per wavelength. The ultrasound time-series signals are then reconstructed into 2D pressure maps using a model-based iterative reconstruction algorithm [28] with a field of view 30 mm × 30 mm and matrix 300 × 300.

B. Magnetic Resonance Imaging

All MRI scans were performed on a 7 T small animal MRI system (Pharmascan, Bruker, Germany). Image acquisition and reconstruction were operated on the ParaVision 6.0 software platform. The T2 MRI images of the nude mouse were obtained using a 2-D spin-echo sequence (Turbo rapid acquisition with refocused echoes) with the following imaging parameters: RARE factor 8, echo time 10 ms, repetition time 6000 ms, 5 averages, slice thickness/gap 0.8/0.2 mm, the field of view 25 mm × 25 mm, matrix 250 × 250, spatial resolution 0.1 mm × 0.1 mm × 0.8 mm.

C. Spatial Co-Registration of the Images of the PAT and MRI Modalities

To achieve dual-modality data acquisition and registration of PAT and MRI in *in vivo* small animals, we developed a novel dual-modality animal imaging bed [27] to ensure that the animal maintains the same spatial positioning and body geometry while switching between the two imaging modalities. The animal bed is designed according to the PAT and MRI system environment and geometric dimensions and is prepared with PLA using a 3D printer (JennyPrinter 4th Generation, Jenny Technology Co., Ltd, China). The dual-modality animal bed consists of a gas tube, a breathing mask, two cylinders, and a solid animal support that can be separated into two parts, one for PAT, and the other for MRI. Moreover, we employed an automated rigid registration algorithm based on contour matching [19]. During registration, the PAT image was set as the fixed image and the MRI image as the moving image, as shown in Fig. 1(b).

D. Simulation Experiment

We first performed a simulation experiment to compare our proposed MRI-OS method and the other two methods (PAT-CS and PAT-OS). Similar to Reference [5], [14], our simulation experiments only incorporate the optical inversion problem that needs to be addressed in this paper, but not the acoustic inversion. We employed a mouse organ model to generate simulation images, as shown in Fig. 3(a). The absorption coefficient of each organ can be calculated by referring to Reference [37]:

$$\mu_a(\lambda) = S (x \mu_{a\text{HbO}_2} + (1 - x) \mu_{a\text{Hb}}) \quad (11)$$

where x was $s\text{O}_2$, S was a scaling factor relative to whole blood. The absorption coefficient μ_a of HbO_2 and Hb at different wavelengths were determined by referring to [5].

Fig. 2 presents the process of obtaining the raw PAT images. We used Toast++ software to simulate the light transport in the object, and then obtained the distribution of LF Φ . As a result, the absorbed energy is proportional to the product of the absorption coefficient and the LF intensity within a given voxel. We multiplied the ideal PAT images μ_a by the LF images Φ to obtain the raw PAT images used in the simulation experiments. We further added noise with a mean of 0 and a standard deviation of 2×10^{-5} to the raw PAT images. In the later LF estimation procedure, the absorption coefficient was

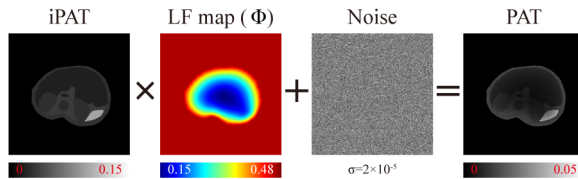


Fig. 2. The process of obtaining the raw PAT images used in the simulation experiment. iPAT: ideal PAT image. LF map (Φ): estimated light fluence distribution using ideal PAT image. Noise: noise with a mean of 0 and a standard deviation of 2×10^{-5} was add to the raw PAT image. PAT: raw PAT image.

initialized to 0 and the scattering coefficient was fixed to the ideal value.

E. Phantom Experiment

We constructed a tissue-mimicking phantom containing rod-shaped inclusions and carried out a PAT imaging experiment to further verify the LF estimation and correction method. The standard and method of making phantom are based on [27], [38]. The background of the phantom was an agar (Aladdin, China) solution mixed with 0.5% Intralipid to enhance scattering. Before its solidification, three 3D printed rod molds were inserted into the background solution. When the solution was cooled and solidified, the molds were pulled out and rod-shaped absorbers containing agar solution mixed with 0.5% Intralipid, 0.02% Chinese ink (Hero, China) and 0.02 g/ml FeCl₃ were inserted. FeCl₃ was included to increase the contrast of MRI images. The diameter of the phantom was 20 mm. PAT images were acquired at a wavelength of 700 nm [Fig. 4]. For the reconstruction, the speed of sound was set to 1500 m/s. In the later LF correction experiment, within each segmentation region, the absorption coefficient μ_a was initialized to 0 and the scattering coefficient μ'_s was fixed to 0.5 mm⁻¹ by referring to Reference [27], [38].

F. Animal Experiment

In the *in vivo* animal imaging experiment, four healthy nude mice (female, 8-weeks, Southern Medical University, Guangzhou, China) were used. Animals were kept in ventilated cages inside a temperature-controlled room, under a 12-h dark/light cycle. In order to reduce abdominal peristalsis artifacts caused by food digestion and to prevent the mice from excreting and polluting the imaging environment during PAT imaging, the nude mice were fasted for 8 hours before imaging. All animal experiments were approved by the local Animal Ethics Committee of Southern Medical University and were performed under current guidelines.

Before the experiment, the nude mice were anesthetized with 4 % chloral hydrate at 0.01 ml/g for fixing. In order to reduce the image artifacts caused by respiratory movements, medical oxygen mixed with high concentration isoflurane (1%, RWD, China) was transmitted through the gas tube to the breathing mask, so that the respiratory rate of nude mice was maintained at 15-20 times/min. For contrast-enhanced PAT imaging, an insulin injection needle was embedded into the tail vein in advance and was connected to a long Polyethylene Tubing 10 (PE 10) that enabled agent injection (ICG)

from outside the imaging chamber. Multispectral PAT images were acquired at five different illumination wavelengths: 700, 730, 760, 800 and 850 nm and averaged with signals from 10 frames per wavelength. For the reconstruction, the speed of sound was set to 1536 m/s. Finally, the linear un-mixing algorithm was used to calculate the distribution of HbO₂, Hb, and ICG. In the later LF estimation procedure, the absorption coefficient was initialized to 0 and the scattering coefficient was fixed by referring to Ref [17], [37].

G. Manual Segmentation

We performed manual segmentation to generate prior images used in the LF correction experiment. The manual segmentation was performed for PAT or rMRI image separately, its process could be divided into three steps: 1) marked a series of landmark points on the edge of the mouse surface or organs; 2) performed spline interpolation based on these landmarks to obtain the initial edge; 3) refined the initial edge until the observer is satisfied. To ensure the accuracy of the segmentation as well as to be less subjectively influenced, we asked three experts to perform manual segmentation individually. In the organ segmentation of PAT and rMRI, we do not require which organs must be segmented, but only need to segment the recognizable organs.

H. Image Quality Metrics

The quantitative performance metrics used to evaluate the convergence performance of the correction algorithm and the quality of the restored images include the L2-norm error (Err), the sum of squared error (SSE), the signal-to-noise ratio (SNR), the contrast-to-noise ratio (CNR), the peak signal to noise ratio (PSNR), the structural similarity (SSIM), the mutual information (MI), and the Pearson correlation coefficient (PCC). Here, the product of the absorption coefficient μ_a and the LF distribution Φ used to approximate the raw PAT image is defined as the estimated PAT image (ePAT).

The L2-norm is a metric to evaluate the convergence performance of the correction algorithm by calculating the error between the raw PAT image and the ePAT image. The smaller the error, the more accurate the solution. It is defined as:

$$Err = \left(\sum_{j=1}^N (PAT_j - ePAT_j)^2 \right)^{\frac{1}{2}}, \quad (12)$$

where, ePAT is the estimated PAT image. PAT is the raw PAT image and N is the total pixel number of the image.

The SSE is defined as:

$$SSE = \sum_{j=1}^N (iPAT_j - cPAT_j)^2, \quad (13)$$

where, iPAT and cPAT are the ideal PAT image and the corrected PAT image, respectively.

The SNR provides a measure of the smoothness of a Region-Of-Interest (ROI) within the imaged object [28], which is defined as:

$$SNR = 10 \cdot \log_{10} \left[\frac{E(x_t)^2}{E([x_t - E(x_t)])^2} \right], \quad (14)$$

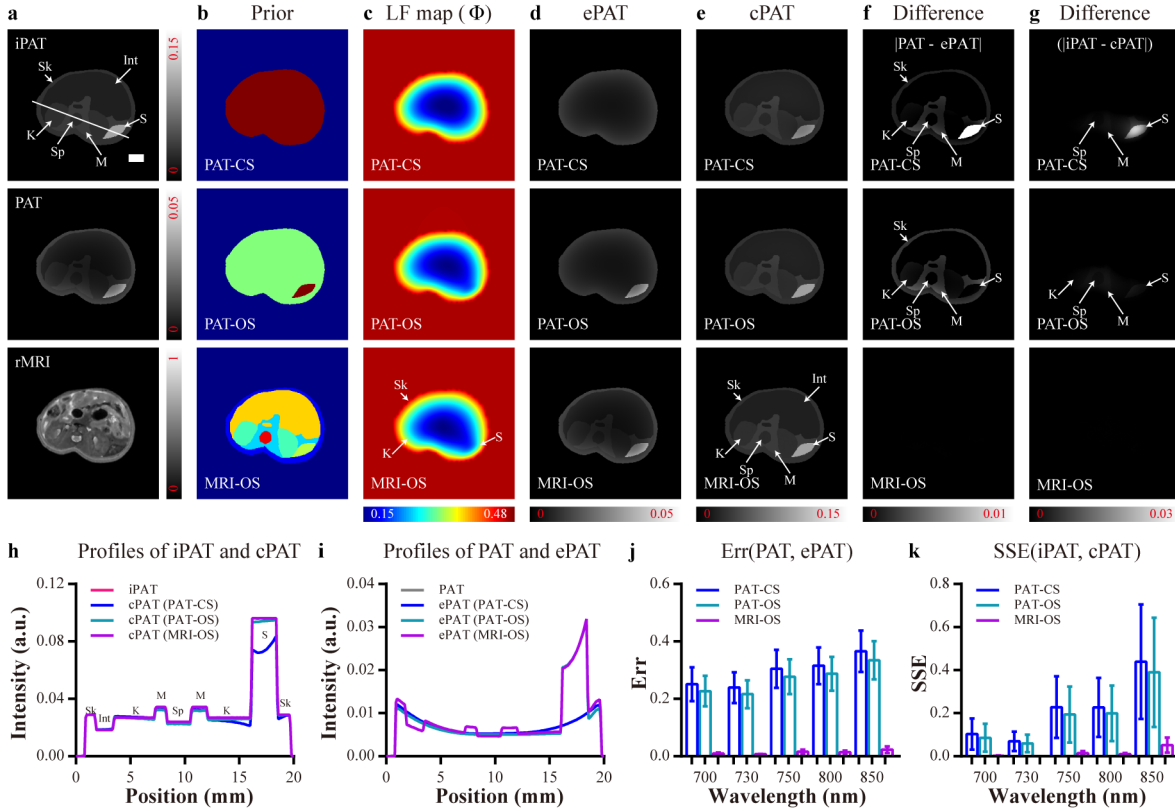


Fig. 3. Simulation LF correction experiment: (a) iPAT: ideal PAT image at 850 nm. PAT: raw PAT image at 850 nm obtained by multiplying the ideal PAT image with the LF map. rMRI: registered MRI image. (b) Prior: segmentation result. (c) LF map (Φ): light fluence distribution map estimated using different methods. (d) ePAT: estimated PAT image derived by using different methods. (e) cPAT: corrected PAT image obtained by using different methods. (f) Difference: the difference images between PAT and ePAT images. (g) Difference: the difference images between iPAT and cPAT images. (h) Profiles of iPAT and cPAT images drawn along the white solid line in (a). (i) Profiles of PAT and ePAT images drawn along the white solid line in (a). (j) The Err values between PAT and ePAT for all positions. Mean \pm SEM. (k) The SSE values between iPAT and cPAT images for all positions. Mean \pm SEM. Description of markers in (a-g): Sk: skin; Int: intestines; K: kidney; Sp: spine; M: muscle; S: spleen. Scale bar, 3 mm.

where x_t is the image restricted to the target ROI and $E(\cdot)$ stands for a spatial average over the ROI.

The CNR is calculated as the mean value difference between the target ROI and the background ROI divided by the standard deviation of the background ROI, given by:

$$CNR = \frac{|\bar{x}_t - \bar{x}_b|}{\sigma_b}, \quad (15)$$

where \bar{x}_t and \bar{x}_b are the mean value of the target ROI and the background ROI, respectively, and σ_b is the standard deviation of the background ROI.

The PSNR is defined as:

$$PSNR = 10 \cdot \log_{10} \left(\frac{L^2}{MSE} \right), \quad (16)$$

where L is the dynamic range of the pixel value ($L = 255$ for 8 bits grayscale images).

The SSIM measured the similarity between the restored image and the rMRI image in terms of brightness (mean image intensity), contrast (intensity variance), and structure (intensity covariance). It is defined as:

$$SSIM = \frac{(2\mu_I\mu_x + C_1)(2\sigma_{I,x} + C_2)}{(\mu_I^2 + \mu_x^2 + C_1)(\sigma_I^2 + \sigma_x^2 + C_2)}, \quad (17)$$

where, μ_I and μ_x are the mean of the rMRI image I and the restored image x , respectively. σ_I^2 and σ_x^2 are the variance of

I and x , respectively. $\sigma_{I,x}$ is the covariance of the image I and x . The small constants C_1 , C_2 and C_3 are given by:

$$C_1 = (K_1 L)^2, \quad C_2 = (K_2 L)^2, \quad C_3 = C_2/2, \quad (18)$$

where, K_1 and K_2 are set as $K_1 = 0.01$ and $K_2 = 0.03$ respectively.

The MI is a metric to quantify the interdependence between the rMRI image and the restored image. It is defined as:

$$MI = H(I) + H(x) - H(I, x), \quad (19)$$

where $H(I)$ and $H(x)$ denotes the entropy of the rMRI image and the restored image, and $H(I, x)$ denotes the joint entropy of these images.

The PCC is a metric to quantify the degree of correlation between the rMRI image and the restored image. It is defined as:

$$PCC = \frac{\sigma_{I,x}}{\sqrt{\sigma_I^2 \sigma_x^2}} \quad (20)$$

I. Statistical Analysis

SPSS Statistics software (IBM) was used for one-way ANOVA (followed with Sidak multiple comparisons test) statistical analysis.

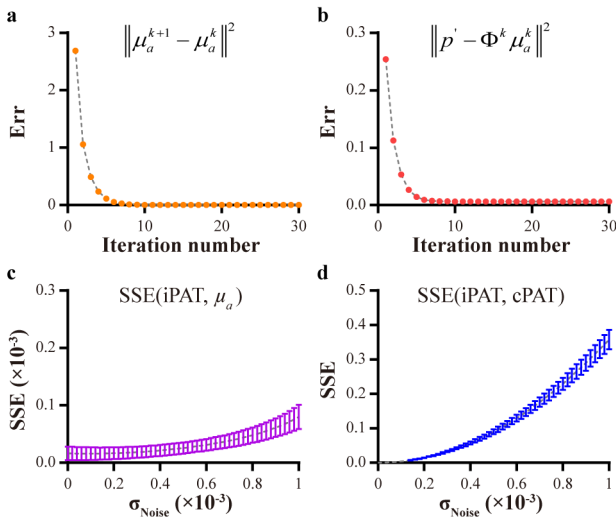


Fig. 4. Measure of method performance. (a) Err between two adjacent iterative values as a function of the number of iterations. (b) Err between PAT and ePAT as a function of the number of iterations. (c) SSE between iPAT and absorption coefficient μ_a as a function of noise standard deviation. Mean \pm SEM. (d) SSE between iPAT and cPAT as a function of noise standard deviation. Mean \pm SEM.

IV. LF CORRECTION RESULTS

A. Simulation Results

Firstly, we performed a simulation LF correction experiment to compare the performance between our proposed MRI-OS method and the other two methods. The LF correction procedures of all three methods were solved by our proposed two-step iterative optimization algorithm. The LF correction results of the simulation experiment are shown in Fig. 3. In the ideal PAT image (iPAT), each organ has a uniform signal intensity, as shown in Fig. 3(a). However, due to the attenuation of laser energy in the transmission process, the PAT signal weakens with the increase of imaging depth. The registered MRI image (rMRI) is shown in Fig. 3(a). The prior images of the LF correction are shown in Fig. 3(b). For the PAT-CS, PAT-OS, and our proposed methods, the segmentation is carried out by segmenting the object contour from the PAT image, segmenting the spleen from the PAT image, and segmenting the skin, kidneys, spine, muscle, spleen, and intestines from the rMRI image, respectively.

Based on the segmentation results, the LF maps, the estimated PAT images (ePAT), and the corrected PAT images (cPAT) obtained by different methods are shown in Fig. 3(c-e). As can be seen from the cPAT images, all three methods can enhance the signal from deeper tissues. And similar to PAT image, ePAT images obtained from all three methods also have signal attenuation with depth. However, in the PAT-CS method, because of the uniform absorption coefficient, the signal within the same organ of the cPAT image is still inhomogeneous (e.g. spleen) and the ePAT did not coincide with the PAT images. The PAT-OS method improves the signal inhomogeneity within the spleen. Furthermore, the cPAT image obtained by the MRI-OS method not only compensates for the low signal at larger depth but also enhances the signal of the spleen [Fig. 3(e)].

We have calculated the difference between PAT and ePAT, iPAT and cPAT images. The results are shown in Fig. 3(f, g). It can be observed that the difference in the LF correction results with the PAT-CS method is large at organs with high absorption coefficients (such as kidneys and spleen). The results obtained by the PAT-OS method have smaller difference in the spleen, but not in the muscle. In contrast, the difference in the LF correction results obtained with the MRI-OS method is the smallest in all organs. For further comparison, Fig. 3(h, i) show the image profiles of the iPAT, cPAT, PAT and ePAT. The position of the profiles is along the white solid line in Fig. 3(a). The profiles show the highest degree of overlap between the iPAT and cPAT, PAT and ePAT obtained by the MRI-OS method [Fig. 3(h,i)]. The above results indicate that the LF correction with accurate organ segmentation can better compensate for the influence of the inhomogeneous distribution of the light energy.

Next, we measured the Err between the entire PAT and ePAT images, the SSE between the entire iPAT and cPAT images in the simulation experiment for all positions and all wavelengths, and the results are shown in Fig. 3(j, k). For the Err results of 850 nm, compared with the PAT-CS method, the MRI-OS method was reduced by 93.73%, while the PAT-OS method was reduced by 8.53%. For the SSE results of 850 nm, compared with the PAT-CS method, the MRI-OS method reduced the SSE value by 88.28%, while PAT-OS method reduced by 11.20%. For both the Err and SSE results at all wavelengths, MRI-OS LF correction can get the smallest values compared with other methods.

Fig. 4(a, b) shows the Err values with respect to different iteration numbers. We can see that the algorithm is sufficient to reach convergence within 10 iterations. Fig. 4(c, d) shows the SSE values with respect to different noise standard deviations. The SSE between iPAT and the calculated absorption coefficient μ_a is small, indicating that our algorithm is able to solve the absorption coefficients with small errors in noisy PAT images [Fig. 4(c)]. Since cPAT images contain noise, the SSE between iPAT and cPAT images increases with the noise standard deviation [Fig. 4(d)].

Furthermore, we acquired the HbO_2 and Hb images and calculated the sO_2 images, and the results are shown in Fig. 5(a-e). The image profiles of HbO_2 , Hb and sO_2 are illustrated in Fig. 5(f). The position of the profiles is along the white solid line in Fig. 5(a). As can be seen from the uncorrected results, the light energy attenuation process affects the spectral un-mixing, resulting in decrease signal with the increase of depth in the HbO_2 and Hb images [Fig. 5(b)]. This further leads to varying sO_2 values within the same organ (contrary to the ideal value) [Fig. 5(b)]. The PAT-CS and PAT-OS methods enhance the concentrations of HbO_2 and Hb in the deep regions of the image [Fig. 5(c, d)], but failed to accurately compensate for the LF in the kidneys, muscle, spine and spleen, leading to errors in the sO_2 of these regions. The MRI-OS method brings the concentrations of HbO_2 and Hb in each organ to a uniform distribution, and the sO_2 values are consistent with the ideal values [Fig. 5(e)]. The image profiles in Fig. 5(f) also show the accuracy of LF correction of the

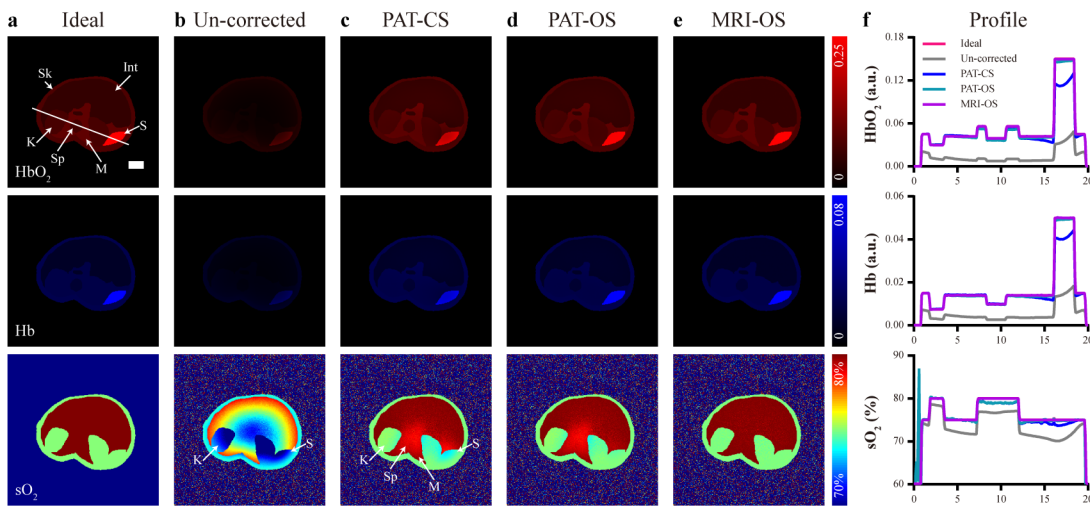


Fig. 5. Spectral un-mixing results of simulation experiment: (a-e) The HbO_2 , Hb concentration distribution and sO_2 images obtained by spectral un-mixing from ideal, un-corrected and cPAT images. (f) Profiles of HbO_2 , Hb and sO_2 drawn along the white solid line in (a). Description of markers: Sk: skin; Int: intestines; K: kidney; Sp: spine; M: muscle; S: spleen. Scale bar, 3 mm.

MRI-OS method, as evidenced by the high overlap with the ideal profiles.

B. Phantom Experiment Results

The LF correction results of the tissue-mimicking phantom imaging experiment are shown in Fig. 6. In the raw PAT image [Fig. 6(a)], the signal intensity of the inner rod is lower than that of the two outer rods due to the attenuation of light. The prior images of the three methods are shown in Fig. 6(b). For the PAT-CS method, only the background is segmented from the PAT image. For the PAT-OS method, the background and absorbers are segmented from the PAT image. For our MRI assisted method, the background and absorbers are segmented from the rMRI image. In both the PAT-CS and PAT-OS methods, the unclear object boundary makes the segmentation result inaccurate (not a smooth circle). In contrast, circular absorbers and background can be easily segmented in the rMRI image by using thresholding [Fig. 6(b)].

Fig. 6(c, d) show the LF maps and ePAT images estimated using different methods. Compared with the PAT-CS method, the LF maps obtained by the PAT-OS and MRI-OS methods show rapid LF decay in the rod-shaped absorbers [Fig. 6(c)]. Similar to the raw PAT image, the ePAT images derived from all three methods have signal attenuation with increasing imaging depth [Fig. 6(d)]. However, the ePAT images derived from the PAT-OS and MRI-OS methods [Fig. 6(d)] are similar to the original PAT image in Fig. 6(a): the signal intensity of the inner rod is lower than that of the two outer rods. Further, the LF corrected PAT images (cPAT) are shown in Fig. 6(e). In the cPAT image [Fig. 6(e)] obtained by the MRI-OS method, the three rod-shaped absorbers have very similar pixel values, and within each absorber, the pixel values become more homogeneous.

For further comparison, the image profiles of PAT, ePAT and cPAT at the position along the white solid line in Fig. 6(a) are illustrated in Fig. 6(f, g). The profile shows a higher degree of similarity between the PAT and ePAT obtained by

the MRI-OS method, and the PAT signal of the two outer rod-shaped absorbers decreases with depth [Fig. 6 (f)]. The profile of the cPAT image obtained by the MRI-OS method shows that the intensity of these three rod-shaped inclusions have reached the same level, and the intensity of the two outer absorbers have become more homogeneous [Fig. 6(g)]. In contrast, the outer absorber signal of cPAT obtained by PAT-CS and PAT-OS methods is still higher than that of the inner side (as indicated by the red arrow).

C. Animal Results

Fig. 7 shows the results of *in vivo* imaging of nude mice at 760 nm, where deoxyhemoglobin absorption dominates. The raw PAT image (PAT) and the registered MRI images (rMRI) are shown in Fig. 7(a). The PAT signal is attenuated in the central features (artery, inferior vena cava (IVC), the interior of the kidney) due to the attenuation of the laser energy. The absorption coefficients μ_a , LF distribution maps, and the corrected PAT images (cPAT) using different methods are shown in Fig. 7(c-e) respectively, and their segmentation prior images are shown in Fig. 7(b). Fig. 7(f) shows the profiles of the LF maps at the position along the white solid line in Fig. 7(d). As can be seen, the LF maps also have an attenuated signal with the increasing imaging depth [Fig. 7(c, f)]. In the PAT-CS method [Fig. 7(c)], the uniform absorption coefficient causes isotropic signal attenuation. In contrast, the LF map estimated by the PAT-OS and MRI-OS methods has a rapid decay in the kidney [Fig. 7(c, f)]. Moreover, affected by the spleen located on the right side of the image, the LF map estimated by the MRI-OS method presents an asymmetric distribution (the attenuation on the right side is more severe) [Fig. 5(c, f)]. This is because the kidney, spleen, and other blood-rich organs have high optical absorption at 760 nm. The results obtained by PAT-CS and PAT-OS methods cannot correctly reflect this phenomenon. Finally, in the cPAT images [Fig. 7(e)], the central features (aorta, IVC, the interior of the kidney, and spine) have been significantly enhanced by all three methods.

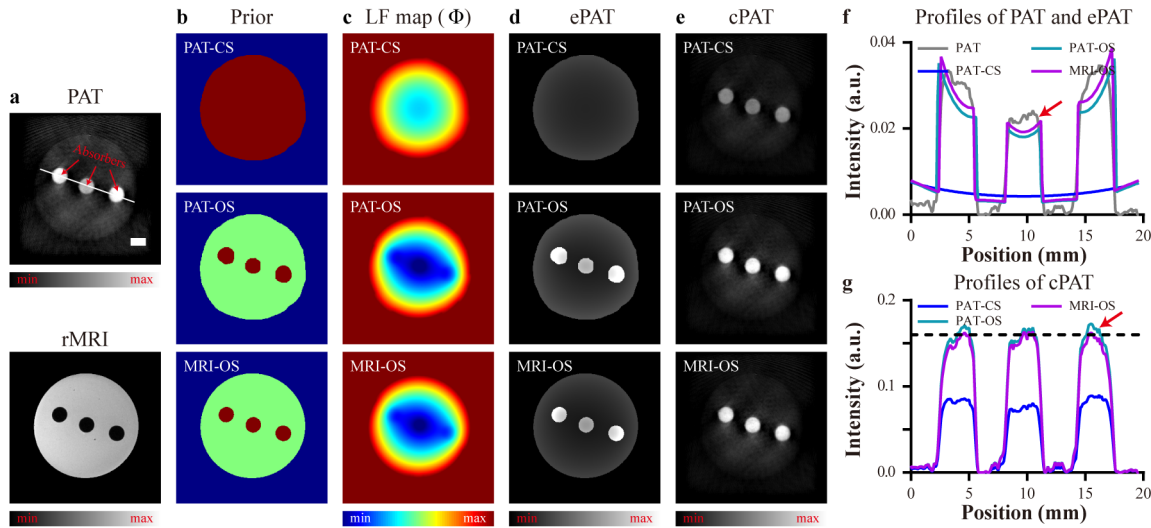


Fig. 6. Tissue-mimicking phantom LF correction experiment: (a) PAT: raw PAT image. rMRI: registered MRI image. (b) Prior: segmentation result of different methods. (c) LF map (Φ): light fluence distribution map estimated using different methods. (d) ePAT: estimated PAT image derived by using different methods. (e) cPAT: corrected PAT image obtained by using different methods. (f) Profiles of PAT and ePAT drawn along the white line in (a). (g) Profiles of cPAT images drawn along the white line in (a). Scale bar, 3 mm.

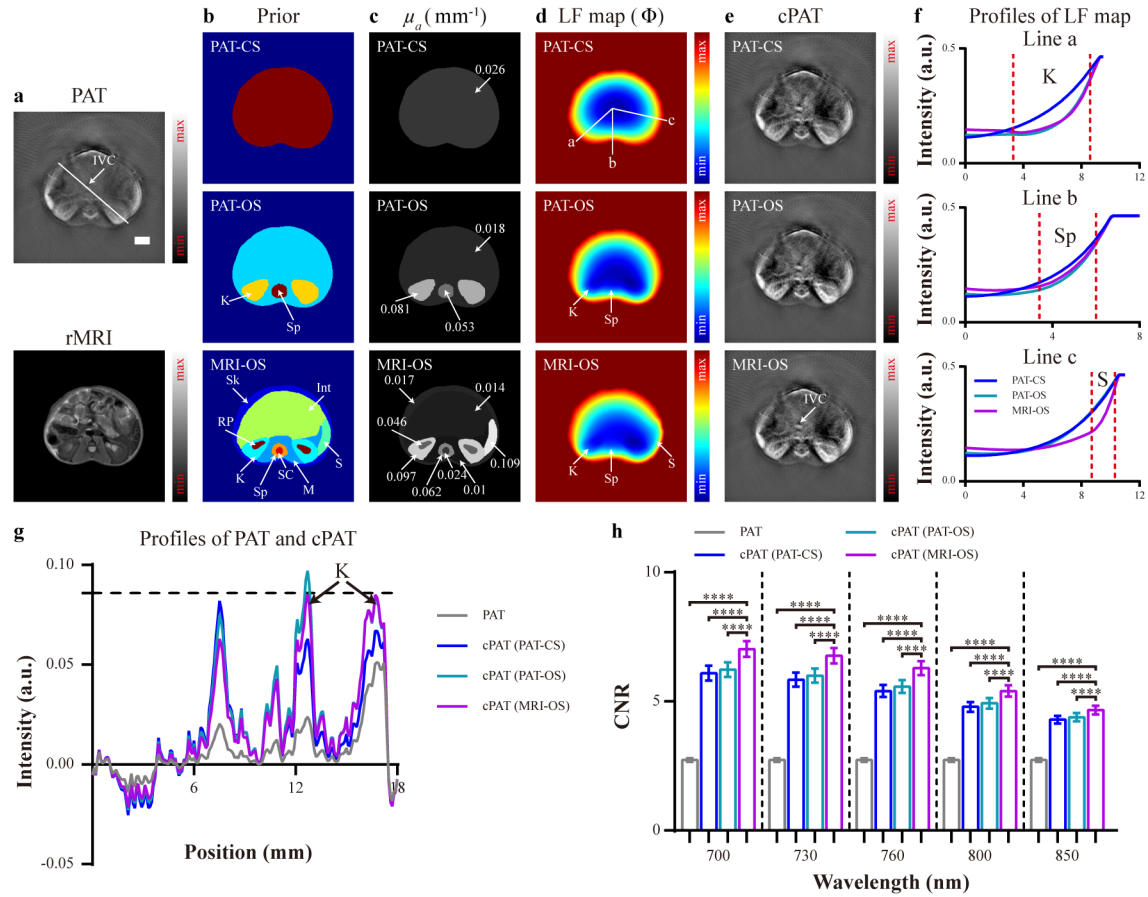


Fig. 7. *In vivo* animal LF correction experiment. (a) PAT: raw PAT image. rMRI: registered MRI image. (b) Prior: segmentation result. (c) μ_a : absorption coefficients solved by different methods. (d) LF map (Φ): light fluence distribution map solved by different methods. (e) cPAT: corrected PAT image obtained by using different methods. (f) Profiles of LF map along the white solid line in (d). (g) Profiles of PAT and cPAT images along the white solid line in (a). (h) The CNR of PAT and cPAT images at different wavelengths. Mean \pm SEM. ***: $P < 0.0001$. Description of markers in (a-e): IVC: inferior vena cava; Sk: skin; Int: intestines; K: kidney; RP: renal pelvis; Sp: spine; SC: spinal cord; M: muscle; S: spleen. Scale bar, 3 mm.

To further assess the performance of these three methods, the profiles of PAT and cPAT along the white solid line in Fig. 7(a) are illustrated in Fig. 7(g). In the profile of the PAT

image, the signal in the superficial layer of the right kidney (K arrows) is higher than that in the deeper layers. In the PAT-CS method, there is still a difference in the profile

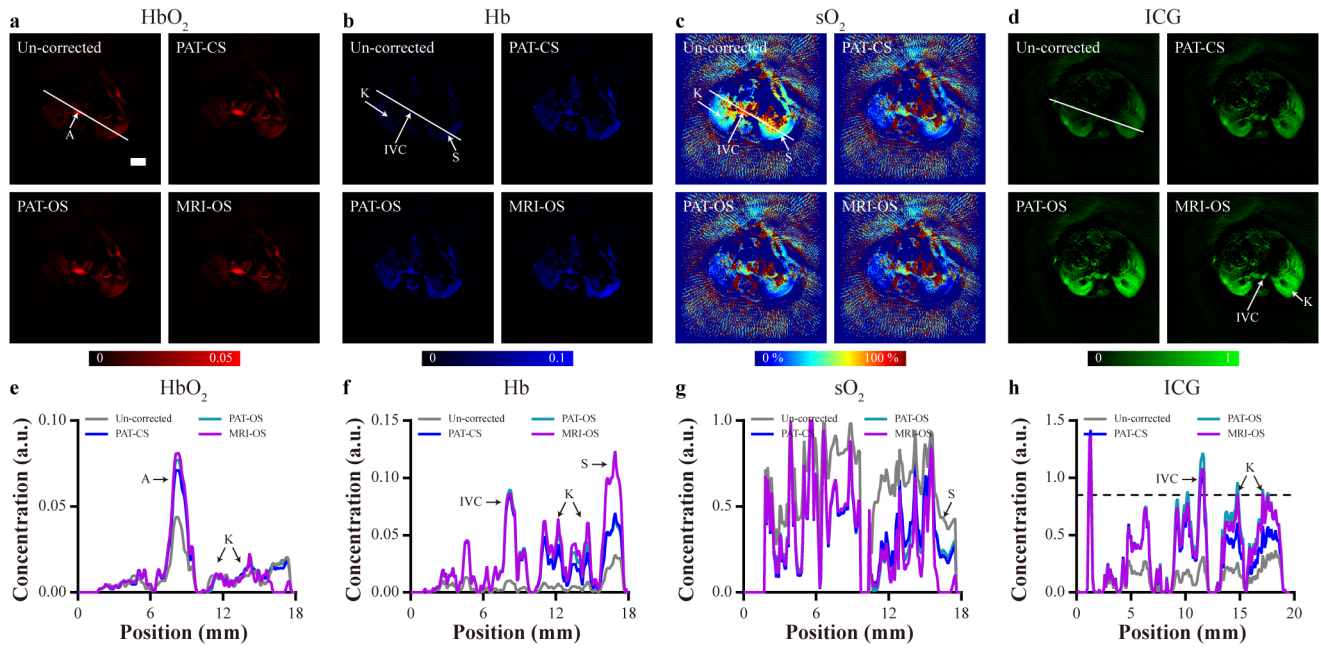


Fig. 8. Spectral un-mixing results of *in vivo* animal experiment: (a-c) The concentration distribution (HbO_2 , Hb) and sO_2 images obtained by spectral un-mixing from the PAT and cPAT images. (d) The concentration distribution images of ICG at the kidney position. (e-h) Profiles of HbO_2 , Hb , sO_2 and ICG along the white solid line in (a-d). A: artery; IVC: inferior vena cava; K: kidney; S: spleen. Scale bar, 3 mm.

amplitudes within the right kidney. This can be improved by segmenting the kidney region in the PAT-OS method, but the internal signal in the kidney has become much higher than the outer region. In our proposed MRI-OS method, there is no obvious difference in the profile amplitudes within the right kidney, and the signal amplitude of the central IVC is also increased. Furthermore, we measured the Err between the entire PAT and ePAT image, and the results are listed in TABLE I. It can be seen that for the LF correction results, the PAT-OS method achieves smaller error than the PAT-CS method (decreased by 2.52%, $P < 0.05$), while our proposed MRI-OS method has the smallest error (decreased by 5.46%, $P < 0.001$).

Next, we measured the CNR of the target and background regions at different wavelengths in *in vivo* animal experiment, and the results are shown in Fig. 7(h). Compared to PAT, cPAT images have higher CNR values, indicating that LF correction enhances the PAT signal in the target region. Among all the methods, the CNR values of our proposed method are the highest at all wavelengths. Specifically, at 700 nm, the CNR of the PAT-CS method and PAT-OS method increased by 123.32% and 128.27% respectively, while our method achieved the highest CNR increase of 157.37%.

Fig. 8(a-c) shows the HbO_2 , Hb , and sO_2 distribution images. The profiles of HbO_2 , Hb , and sO_2 are shown in Fig. 8(e-g). The Hb of hypoxic (the IVC) blood vessels should be higher than other tissues, but these features are not reflected in the un-corrected images due to the laser energy attenuation [Fig. 8(b, f)]. This further leads to increased sO_2 value with increasing depth [Fig. 8(c, g)]. In the HbO_2 and Hb images obtained by the MRI-OS method, the concentrations of HbO_2 and Hb in the depth of the image are enhanced and all blood vessels are visible [Fig. 8(a, b)]. As can be seen from the profiles [Fig. 8(e, f)], the Hb concentration in the IVC,

TABLE I
THE ERR VALUES BETWEEN PAT AND ePAT FOR ALL IMAGE SLICES IN THE *in vivo* ANIMAL EXPERIMENT

Metrics	PAT-CS	PAT-OS	MRI-OS
Err	3.57 ± 0.3	3.48 ± 0.31	3.38 ± 0.28

kidney, and spleen have increased. As a result, the sO_2 values at the kidney and spleen obtained by the MRI-OS method are decreased [Fig. 8(g)].

The results of the ICG experiment are shown in Fig. 8(d). The ICG is metabolized from the veins into the liver, kidneys, and spleen, and thus these regions should have high signal. However, in the un-corrected spectral un-mixing results, the ICG concentration in the kidney is not uniform (inside is lower than the outside), and the ICG signal of the IVC is very weak. In contrast, the cPAT un-mixing results obtained by the MRI-OS method showed enhanced visualization of deep ICG concentration including the IVC and kidneys. Furthermore, the image profiles of ICG along the white solid line in Fig. 8(d) are illustrated in Fig. 8(h). It can be seen that the signal of the IVC at the center of the profile of the PAT image is very low, and the signal of the internal kidney is lower than the external region. The IVC signal of the cPAT image obtained by the MRI-OS LF correction has been significantly enhanced, and the internal and external signals of the kidney have reached the same level [Fig. 8(h)]. These results indicate that our method can help restore the absorber concentration distribution.

V. IMAGE RESTORATION RESULTS

A. Phantom Results

Firstly, we performed the image restoration experiment in the tissue-mimicking phantom, and the results are shown in

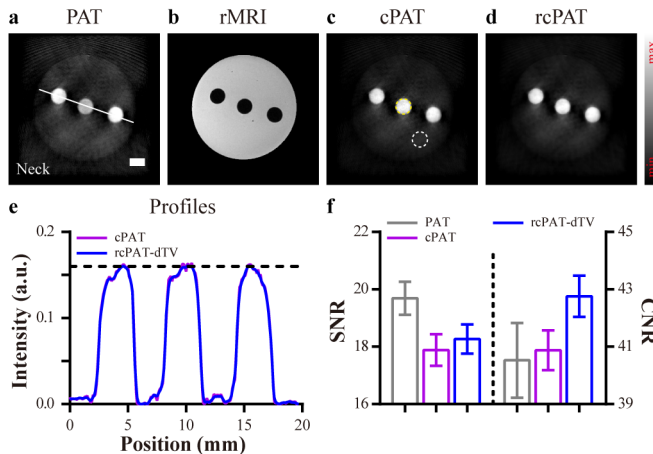


Fig. 9. Tissue-mimicking phantom image restoration experiment. (a) PAT: raw PAT image. (b) rMRI: registered MRI images. (c) cPAT: corrected PAT image. (d) rcPAT: image restored by the dTV method. (e) Profiles of cPAT and rcPAT images drawn along the white solid line in (a). (f) The SNR and CNR of PAT, cPAT and rcPAT images. Mean \pm SEM. Scale bar, 3 mm.

Fig. 9. Fig. 9(a-d) shows the raw PAT images (PAT), registered MRI images (rMRI), corrected PAT images (cPAT), and restored cPAT images using the dTV method (rcPAT). The image profiles are shown in Fig. 9(e), and the SNR and CNR results are shown in Fig. 9(f). The SNR was obtained from the yellow dashed-line target ROI in Fig. 9(c). The CNR was obtained from the yellow dashed-line target ROI and the white dashed-line background ROI in Fig. 9(c). As can be seen, the profiles of rcPAT and cPAT are coincident but smoother, indicating that the image restored by combining the rMRI image can reduce noise while keeping the structural integrity [Fig. 9(e)]. The SNR and CNR of rcPAT were higher than those of cPAT [Fig. 9(f)], which also supported the above conclusion.

B. Animal Results

Next, the image restoration of *in vivo* imaging study of the mouse neck and kidney regions was carried out. Fig. 10 shows the raw PAT images (PAT), corrected PAT images (cPAT), registered MRI images (rMRI), and restored cPAT images using the dTV method (rcPAT) at the neck and kidney positions of the mouse. The regions enclosed by the red boxes in Fig. 10(a, b) are shown as enlarged views. Comparing these images, we can see that the LF correction not only restores the internal signal of the image but also enlarges the noise and artifact. Using the directional gradient information of MRI as a priori, the rcPAT image shows smooth and generates fewer streaking artifacts. The result of the neck shown in Fig. 10(a) shows that our proposed method not only retains the sharp edges of the vessels but also enhances contrast. In addition, there are almost no obvious streaking artifacts in the restored image, whereas in both the raw PAT image and the corrected PAT image these artifacts are prominent. The kidney image obtained by our method shows clear contour, smooth image, complete details, and almost no noise, indicating successful incorporation of the rich soft-tissue information from MRI [Fig. 10(b)]. As can be seen from the results of the profiles

TABLE II
THE SNR AND CNR OF PAT IMAGE RESTORATION RESULTS

Metrics	PAT	cPAT	rcPAT
SNR (dB)	23.55 ± 3.67	18.30 ± 1.92	19.46 ± 2.25
CNR	29.89 ± 3.15	32.37 ± 3.15	40.58 ± 1.42

TABLE III
QUANTITATIVE ANALYSIS OF THE RESTORATION RESULTS FOR THE QUALITY MEASURES

Metrics	cPAT	rcPAT
PSNR (dB)	18.94 ± 2.01	19.23 ± 2.07
SSIM	0.77 ± 0.03	0.78 ± 0.03
MI	0.65 ± 0.05	0.66 ± 0.04
PCC	0.74 ± 0.08	0.75 ± 0.08

in Fig. 10(c, d), compared with the corrected PAT image, our method smooths the image (with smoother curves) and simultaneously preserves gradient details (as the overlapping peaks indicated by the red arrows).

C. Quantitative Results

Quantitative evaluation of the above animal experiment has been carried out. The SNR was obtained from the yellow dashed-line target ROI in Fig. 10. The CNR was obtained from the yellow dashed-line target ROI and the white dashed-line background ROI in Fig. 10. The results are listed in TABLE II. Compared to PAT, cPAT had a higher CNR (+8.3%, $P < 0.01$) and lower SNR (-22.3%, $P < 0.01$), indicating that LF correction amplifies the noise while enhancing the PAT signal in the target region. Compared to cPAT, the CNR of rcPAT increased by 25.36% ($P < 0.0001$), and the SNR increased by 6.34% ($P < 0.001$), indicating that the combined MRI information for image restoration can reduce the noise in the target region and the background region.

TABLE III lists the quantitative analysis results by using rMRI images as reference images, and the best values are marked in bold. As could be seen, the rcPAT results reached a maximum value of 21.69 dB and saw an averaged 1.53% increase in PSNR compared to the cPAT results. This means that the restoration image obtained by our method has lower noise and artifacts. Moreover, the SSIM, MI, and PCC achieved an average increase of 1.3%, 1.54% and 1.35% respectively. In other words, our method could better protect the image structure in the restoration process.

VI. DISCUSSION

The above experiments have demonstrated the incorporation of MRI information for PAT imaging could achieve improved LF correction and dual-modality joint image restoration. Thanks to the dual-modality imaging bed that helped keep the posture of the animal unchanged for PAT and MRI, MRI images that captured rich soft-tissue contrast were successfully co-registered with the PAT images. Based on this co-registration capability, we showed for the first time

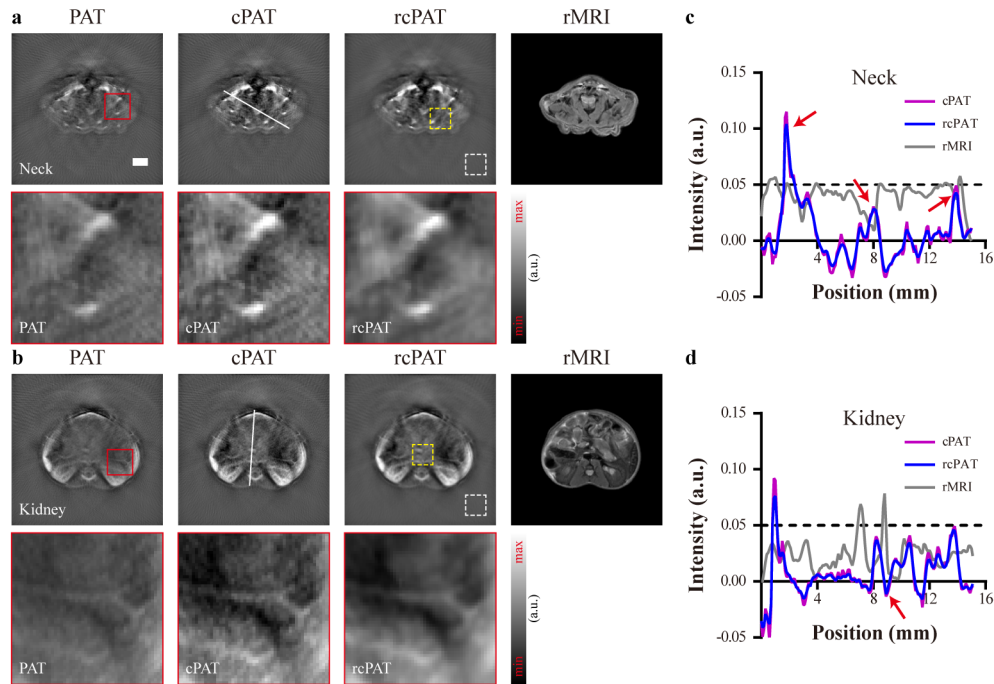


Fig. 10. *In vivo* animal image restoration experiment. (a) PAT image restoration results at the neck position. (b) PAT image restoration results at the kidney position. (c) Profiles of PAT, cPAT, and rcPAT images drawn along the white solid line in (a). (d) Profiles of PAT, cPAT, and rcPAT images drawn along the white solid line in (b). The enlarged regions enclosed in the solid red box are shown. PAT: raw PAT images. cPAT: corrected PAT images. rcPAT: image restored by the dTV method. rMRI: registered MR images. Scale bar, 3 mm.

the introduction of MRI structural information for PAT LF correction and image restoration.

In terms of LF correction, firstly, the organ level segmentation obtained from MRI was acted as prior structural information, which was later incorporated into the LF estimation process. This not only improved the accuracy of organ segmentation, but also assisted the estimation of a more accurate LF distribution map. Our *in vivo* studies indicated that simple manual segmentation on MRI-T2 images with organ boundary recognizable was feasible for improving PAT LF correction.

By incorporating the directional gradient information of the co-registered MRI images, the proposed regularized PAT image restoration method successfully improved PAT image quality. Moreover, as proved by the experimental results of PAT-MRI imaging of multiple organs, exploiting the MRI structural information also benefited the restoration of the LF corrected PAT images. This indicated that the MRI information might be used to help locate and quantify targeted chromophores imaged by multispectral PAT.

In order to facilitate the LF estimation, in our current study, we assumed that the scattering coefficients of different organs were known. However, in real-life situations, the tissue scattering coefficients are spatially variable and should be accountable during LF correction. Also, the structural information provided by the MRI image was based on simple manual segmentation of different organs. This can be improved by using atlas-based automatic segmentation algorithms such as [39] to promote information sharing between MRI and PAT. Finally, anatomical information can also be derived from another imaging modality such as ultrasound. However, the

excellent soft-tissue contrast provided by MRI makes it a unique choice for introducing structural information into PAT.

VII. CONCLUSION

In PAT, the initial laser energy is inhomogeneous due to the absorption of tissue in the process of light propagation, making it difficult to quantitatively analyze the concentration of chromophores at different depths. In this work, we proposed a method of LF correction and image restoration for PAT based on a spatially co-registered MRI image. By conducting simulation, phantom, and *in vivo* small animal imaging experiments, we demonstrated that the PAT image quality could be improved by incorporating the MRI images as prior knowledge to the process of PAT LF correction and image restoration. The proposed method will find its applications in photoacoustic molecular imaging, tumor microenvironment screening, and cancer metastasis tracking since it offers more precise spatial-temporal localization of targeted lesions.

REFERENCES

- [1] L. V. Wang and J. Yao, "A practical guide to photoacoustic tomography in the life sciences," *Nature Methods*, vol. 13, no. 8, pp. 38–627, Jul. 2016, doi: [10.1038/nmeth.3925](https://doi.org/10.1038/nmeth.3925).
- [2] L. V. Wang and S. Hu, "Photoacoustic tomography: *In vivo* imaging from organelles to organs," *Science*, vol. 335, no. 6075, pp. 62–1458, Mar. 2012, doi: [10.1126/science.1216210](https://doi.org/10.1126/science.1216210).
- [3] L. Nie and X. Chen, "Structural and functional photoacoustic molecular tomography aided by emerging contrast agents," *Chem. Soc. Rev.*, vol. 43, no. 20, pp. 70–7132, 2014, doi: [10.1039/c4cs00086b](https://doi.org/10.1039/c4cs00086b).
- [4] S. Tzoumas, N. Deliolanis, S. Morscher, and V. Ntziachristos, "Unmixing molecular agents from absorbing tissue in multispectral optoacoustic tomography," *IEEE Trans. Med. Imag.*, vol. 33, no. 1, pp. 48–60, Jan. 2014, doi: [10.1109/TMI.2013.2279994](https://doi.org/10.1109/TMI.2013.2279994).

- [5] X. Li *et al.*, "Multispectral interlaced sparse sampling photoacoustic tomography," *IEEE Trans. Med. Imag.*, vol. 39, no. 11, pp. 3463–3474, Nov. 2020, doi: [10.1109/TMI.2020.2996240](https://doi.org/10.1109/TMI.2020.2996240).
- [6] S. Mallidi, G. P. Luke, and S. Emelianov, "Photoacoustic imaging in cancer detection, diagnosis, and treatment guidance," *Trends Biotechnol.*, vol. 29, no. 5, pp. 21–213, May 2011, doi: [10.1016/j.tibtech.2011.01.006](https://doi.org/10.1016/j.tibtech.2011.01.006).
- [7] S. Zhang *et al.*, "Photoacoustic imaging of living mice enhanced with a low-cost contrast agent," *Biomed. Opt. Exp.*, vol. 10, no. 11, pp. 5744–5754, Nov. 2019, doi: [10.1364/BOE.10.005744](https://doi.org/10.1364/BOE.10.005744).
- [8] P. Beard, "Biomedical photoacoustic imaging," *Interface Focus*, vol. 1, no. 4, pp. 31–602, Aug. 2011, doi: [10.1098/rsfs.2011.0028](https://doi.org/10.1098/rsfs.2011.0028).
- [9] X. Luís Deán-Ben and D. Razansky, "Adding fifth dimension to optoacoustic imaging: Volumetric time-resolved spectrally enriched tomography," *Light, Sci. Appl.*, vol. 3, no. 1, p. e137, Jan. 2014, doi: [10.1038/lsta.2014.18](https://doi.org/10.1038/lsta.2014.18).
- [10] A. Kazakeviciute, C. J. H. Ho, and M. Olivo, "Multispectral photoacoustic imaging artifact removal and denoising using time series model-based spectral noise estimation," *IEEE Trans. Med. Imag.*, vol. 35, no. 9, pp. 2151–2163, Sep. 2016, doi: [10.1109/TMI.2016.2550624](https://doi.org/10.1109/TMI.2016.2550624).
- [11] B. T. Cox, J. G. Laufer, and P. C. Beard, "The challenges for quantitative photoacoustic imaging," *Proc. SPIE*, vol. 7177, p. 717713, Feb. 2009.
- [12] L. Qi *et al.*, "Photoacoustic tomography image restoration with measured spatially variant point spread functions," *IEEE Trans. Med. Imag.*, vol. 40, no. 9, pp. 2318–2328, Sep. 2021, doi: [10.1109/TMI.2021.3077022](https://doi.org/10.1109/TMI.2021.3077022).
- [13] B. T. Cox, J. G. Laufer, P. C. Beard, and S. R. Arridge, "Quantitative spectroscopic photoacoustic imaging: A review," *J. Biomed. Opt.*, vol. 17, no. 6, Jun. 2012, Art. no. 061202, doi: [10.1117/1.JBO.17.6.061202](https://doi.org/10.1117/1.JBO.17.6.061202).
- [14] B. T. Cox, S. R. Arridge, K. P. Köstli, and P. C. Beard, "Two-dimensional quantitative photoacoustic image reconstruction of absorption distributions in scattering media by use of a simple iterative method," *Appl. Opt.*, vol. 45, no. 8, pp. 1866–1875, Mar. 2006, doi: [10.1364/AO.45.001866](https://doi.org/10.1364/AO.45.001866).
- [15] L. Yao, Y. Sun, and H. Jiang, "Quantitative photoacoustic tomography based on the radiative transfer equation," *Opt. Lett.*, vol. 34, no. 12, pp. 7–1765, Jun. 2009, doi: [10.1364/ol.34.001765](https://doi.org/10.1364/ol.34.001765).
- [16] T. Saratoon, T. Tarvainen, B. T. Cox, and S. R. Arridge, "A gradient-based method for quantitative photoacoustic tomography using the radiative transfer equation," *Inverse Problems*, vol. 29, no. 7, Jul. 2013, Art. no. 075006, doi: [10.1088/0266-5611/29/7/075006](https://doi.org/10.1088/0266-5611/29/7/075006).
- [17] F. M. Brochu, J. Brunker, J. Joseph, M. R. Tomaszewski, S. Morscher, and S. E. Bohndiek, "Towards quantitative evaluation of tissue absorption coefficients using light fluence correction in optoacoustic tomography," *IEEE Trans. Med. Imag.*, vol. 36, no. 1, pp. 322–331, Jan. 2017, doi: [10.1109/TMI.2016.2607199](https://doi.org/10.1109/TMI.2016.2607199).
- [18] X. Li *et al.*, "Model-based optoacoustic tomography image reconstruction with non-local and sparsity regularizations," *IEEE Access*, vol. 7, pp. 102136–102148, 2019, doi: [10.1109/ACCESS.2019.2930650](https://doi.org/10.1109/ACCESS.2019.2930650).
- [19] W. Ren, H. Skulason, F. Schlegel, M. Rudin, J. Klohs, and R. Ni, "Automated registration of magnetic resonance imaging and optoacoustic tomography data for experimental studies," *Neurophotonics*, vol. 6, no. 2, Apr. 2019, Art. no. 025001, doi: [10.1117/1.NPh.6.2.025001](https://doi.org/10.1117/1.NPh.6.2.025001).
- [20] R. Ni, M. Vaas, W. Ren, and J. Klohs, "Noninvasive detection of acute cerebral hypoxia and subsequent matrix-metalloproteinase activity in a mouse model of cerebral ischemia using multispectral-optoacoustic-tomography," *Neurophotonics*, vol. 5, no. 1, Jan. 2018, Art. no. 015005, doi: [10.1117/1.NPh.5.1.015005](https://doi.org/10.1117/1.NPh.5.1.015005).
- [21] A. B. Attia *et al.*, "Multispectral optoacoustic and MRI coregistration for molecular imaging of orthotopic model of human glioblastoma," *J. Biophotonics*, vol. 9, no. 7, pp. 8–701, Jul. 2016, doi: [10.1002/jbio.201500321](https://doi.org/10.1002/jbio.201500321).
- [22] Y. Ju *et al.*, "Monodisperse Au–Fe₂C Janus nanoparticles: An attractive multifunctional material for triple-modal imaging-guided tumor photothermal therapy," *ACS Nano*, vol. 11, no. 9, pp. 9239–9248, Sep. 2017, doi: [10.1021/acsnano.7b04461](https://doi.org/10.1021/acsnano.7b04461).
- [23] K. Ke *et al.*, "Copper manganese sulfide nanoplates: A new two-dimensional theranostic nanoplateform for MRI/MSOT dual-modal imaging-guided photothermal therapy in the second near-infrared window," *Theranostics*, vol. 7, no. 19, pp. 4763–4776, 2017, doi: [10.7150/thno.21694](https://doi.org/10.7150/thno.21694).
- [24] C. W. Hupple, S. Morscher, N. C. Burton, M. D. Pagel, L. R. McNally, and J. Cárdenas-Rodríguez, "A light-fluence-independent method for the quantitative analysis of dynamic contrast-enhanced multispectral optoacoustic tomography (DCE MSOT)," *Photoacoustics*, vol. 10, pp. 54–64, Jun. 2018, doi: [10.1016/j.pacs.2018.04.003](https://doi.org/10.1016/j.pacs.2018.04.003).
- [25] M. Gehring, M. Tomaszewski, D. McIntyre, J. Disselhorst, and S. Bohndiek, "Co-registration of optoacoustic tomography and magnetic resonance imaging data from murine tumour models," *Photoacoustics*, vol. 18, Jun. 2020, Art. no. 100147, doi: [10.1016/j.pacs.2019.100147](https://doi.org/10.1016/j.pacs.2019.100147).
- [26] W. Ren, X. L. Deán-Ben, M. Augath, and D. Razansky, "Development of concurrent magnetic resonance imaging and volumetric optoacoustic tomography: A phantom feasibility study," *J. Biophotonics*, vol. 14, no. 2, Feb. 2021, Art. no. e202000293, doi: [10.1002/jbio.202000293](https://doi.org/10.1002/jbio.202000293).
- [27] S. Zhang *et al.*, "In vivo co-registered hybrid-contrast imaging by successive photoacoustic tomography and magnetic resonance imaging," *BioRxiv*, 2021, doi: [10.1101/2021.03.06.434031](https://doi.org/10.1101/2021.03.06.434031).
- [28] L. Qi *et al.*, "Cross-sectional photoacoustic tomography image reconstruction with a multi-curve integration model," *Comput. Methods Programs Biomed.*, vol. 197, Dec. 2020, Art. no. 105731, doi: [10.1016/j.cmpb.2020.105731](https://doi.org/10.1016/j.cmpb.2020.105731).
- [29] T. Jetzfellner, D. Razansky, A. Rosenthal, R. Schulz, K.-H. Englmeier, and V. Ntziachristos, "Performance of iterative optoacoustic tomography with experimental data," *Appl. Phys. Lett.*, vol. 95, no. 1, Jul. 2009, Art. no. 013703, doi: [10.1063/1.3167280](https://doi.org/10.1063/1.3167280).
- [30] S. Mandal, X. L. Dean-Ben, and D. Razansky, "Visual quality enhancement in optoacoustic tomography using active contour segmentation priors," *IEEE Trans. Med. Imag.*, vol. 35, no. 10, pp. 2209–2217, Oct. 2016, doi: [10.1109/TMI.2016.2553156](https://doi.org/10.1109/TMI.2016.2553156).
- [31] Z. Liang *et al.*, "Automatic 3-D segmentation and volumetric light fluence correction for photoacoustic tomography based on optimal 3-D graph search," *Med. Image Anal.*, vol. 75, Jan. 2022, Art. no. 102275, doi: [10.1016/j.media.2021.102275](https://doi.org/10.1016/j.media.2021.102275).
- [32] M. Schweiger and S. Arridge, "The Toast++ software suite for forward and inverse modeling in optical tomography," *J. Biomed. Opt.*, vol. 19, no. 4, Apr. 2014, Art. no. 040801, doi: [10.1117/1.JBO.19.4.040801](https://doi.org/10.1117/1.JBO.19.4.040801).
- [33] J. Prakash, D. Sanny, S. K. Kalva, M. Pramanik, and P. K. Yalavarthy, "Fractional regularization to improve photoacoustic tomographic image reconstruction," *IEEE Trans. Med. Imag.*, vol. 38, no. 8, pp. 1935–1947, Aug. 2019, doi: [10.1109/TMI.2018.2889314](https://doi.org/10.1109/TMI.2018.2889314).
- [34] X. Li, J. Ge, S. Zhang, J. Wu, L. Qi, and W. Chen, "Multispectral interlaced sparse sampling photoacoustic tomography based on directional total variation," *Comput. Methods Programs Biomed.*, vol. 214, Feb. 2022, Art. no. 106562, doi: [10.1016/j.cmpb.2021.106562](https://doi.org/10.1016/j.cmpb.2021.106562).
- [35] M. J. Ehrhardt and M. M. Betcke, "Multicontrast MRI reconstruction with structure-guided total variation," *SIAM J. Imag. Sci.*, vol. 9, no. 3, pp. 1084–1106, Aug. 2016, doi: [10.1137/15m1047325](https://doi.org/10.1137/15m1047325).
- [36] N. Keshava and J. F. Mustard, "Spectral unmixing," *IEEE Signal Process. Mag.*, vol. 19, no. 1, pp. 44–57, Aug. 2002, doi: [10.1109/79.974727](https://doi.org/10.1109/79.974727).
- [37] G. Alexandrakis, F. R. Rannou, and A. F. Chatzioannou, "Tomographic bioluminescence imaging by use of a combined optical-PET (OPET) system: A computer simulation feasibility study," *Phys. Med. Biol.*, vol. 50, pp. 4225–4241, Sep. 2005, doi: [10.1088/0031-9155/50/17/021](https://doi.org/10.1088/0031-9155/50/17/021).
- [38] R. Cubeddu, A. Pifferi, P. Taroni, A. Torricelli, and G. Valentini, "A solid tissue phantom for photon migration studies," *Phys. Med. Biol.*, vol. 42, no. 10, pp. 9–1971, Oct. 1997, doi: [10.1088/0031-9155/42/10/011](https://doi.org/10.1088/0031-9155/42/10/011).
- [39] M. Cabezas, A. Oliver, X. Lladó, J. Freixenet, and M. B. Cuadra, "A review of atlas-based segmentation for magnetic resonance brain images," *Comput. Methods Programs Biomed.*, vol. 104, no. 3, pp. e158–e177, Dec. 2011, doi: [10.1016/j.cmpb.2011.07.015](https://doi.org/10.1016/j.cmpb.2011.07.015).